JM PAPERS

Evaporation of acoustically levitated bicomponent droplets: mass and heat transfer characteristics

Yuki Wakata[1], Xing Chao[1], Chao Sun[1,2],† and Christian Diddens[3]

[1]New Cornerstone Science Laboratory, Center for Combustion Energy, Key Laboratory for Thermal Science and Power Engineering of Ministry of Education, Department of Energy and Power Engineering, Tsinghua University, 100084 Beijing, PR China

[2]Department of Engineering Mechanics, School of Aerospace Engineering, Tsinghua University, 100084 Beijing, PR China

[3]Physics of Fluids group, Max-Planck Center Twente for Complex Fluid Dynamics, Department of Science and Technology, Mesa + Institute and J. M. Burgers Center for Fluid Dynamics, University of Twente, P.O. Box, 217, 7500 AE Enschede, The Netherlands

Evaporation of multicomponent droplets is important, albeit complex, in a wide range of applications, and requires a careful investigation. We investigate experimentally and numerically the evaporation characteristics of spherical, ethanol–water droplets with different initial concentration ratios in the acoustic levitation field. Imaging techniques and infrared thermometry are used for acquiring volume and surface temperature variations of droplets, reflecting their mass and heat transfer characteristics. Numerical simulations are conducted using modified parameters based on a theoretical model to consider the effect of the acoustic field. The calculation results show good agreement with the experimental data. The concentration and temperature distribution within the droplet is further investigated based on the numerical results.

1. Introduction

Evaporation of spray droplets is ubiquitous in many natural and industrial processes, including spray cooling, inkjet printing, fuel combustion and even virus transmission via saliva droplets (Zang *et al.* 2019; Lieber *et al.* 2021; Lohse 2022). From the most elementary model proposed by Maxwell (1877), which considers the purely diffusive

† Email address for correspondence: chaosun@tsinghua.edu.cn

evaporation of a single spherical droplet, researchers refined various aspects of this problem to be more relevant to reality, considering the effects of the Stefan flow (Fuchs 1959), non-spherical droplets (Tonini & Cossali 2013; Al Zaitone 2018), gas temperature gradient (Tonini & Cossali 2012), and so on. When the system involves two or more components, the evaporation process becomes significantly more complex due to the introduction of additional factors, including the coupling of different component evaporation, thermal and solutal Marangoni flow generated by local concentration gradients, and vapour condensation (Law & Law 1982; Sirignano 1983; Tonini & Cossali 2019; Li, Lohse & Huisman 2023). The evaporation of multicomponent droplets placed on a surface has been investigated extensively by studies such as Diddens *et al.* (2017) and Diddens, Li & Lohse (2021), and is summarised in a recent review by Wang *et al.* (2022). Nevertheless, experimental studies of non-contact spray droplet evaporation are limited due to experimental methodology constraints. Different methods have been designed to investigate droplet evaporation in mid-air, such as measuring directly sprays generated by nozzles (Li *et al.* 2023), or using monodisperse droplet streams generated through Rayleigh-type disintegration (Maqua *et al.* 2008).

The acoustic levitation method has received increasing attention due to its ability to levitate stably the sample fluid of a considerable size for an extended duration without any surface contact (Zang *et al.* 2017; Andrade, Pérez & Adamowski 2018; O'Connell, Sharratt & Cabral 2023). The steady-state geometry and spatial location of an acoustically levitated droplet have been well studied both theoretically and experimentally (Tian, Holt & Apfel 1993; Shi & Apfel 1996; Yarin, Pfaffenlehner & Tropea 1998), while further research is required to understand its evaporation characteristics, which are influenced by the secondary flows introduced by the acoustic field, known as acoustic streaming (Lee & Wang 1990; Riley 2001). Such acoustic streaming includes strong convection close to the droplet interface (inner acoustic streaming) and large-scale toroidal vortices (outer acoustic streaming), which were observed experimentally by Trinh & Robey (1994).

Yarin *et al.* (1999) proposed a theoretical solution for the flow field around an acoustically levitated droplet of pure liquid and the corresponding Sherwood number (the ratio of convective to diffusive mass transfer) for the droplet evaporation. Their theoretical solution has been extended to the evaporation of bicomponent droplets in Yarin, Brenn & Rensink (2002) and has been utilized in a wide range of studies (Al Zaitone & Tropea 2011; Chen *et al.* 2022; Zeng *et al.* 2023). Brenn *et al.* (2007), on the other hand, applied the Lierke (1996) model in conjunction with correlation functions to calculate the Sherwood number and examine the evaporation of multicomponent droplets. Numerical simulations for acoustically levitated droplets have also been investigated (Bänsch & Götz 2018; Doss & Bänsch 2022), but there is currently a lack of studies on multicomponent droplets, and validation with experimental results is also lacking. As the mass and heat transfer are coupled in the evaporation process (Sirignano 2010), additional attention should to be paid to the droplet temperature variation and to perform a quantitative analysis of heat transfer characteristics in the acoustic field. In this regard, Sasaki *et al.* (2020) measured the temperature variation of bicomponent droplets, and obtained the heat transfer coefficients. Further investigation is needed to interpret these coefficients mechanistically and investigate the coupling of heat and mass transfer. Moreover, it is worth noting that some studies (e.g. Yarin *et al.* 1999, 2002; Al Zaitone & Tropea 2011) utilised ventilation flow to eliminate vapour accumulation in the vortices of outer acoustic streaming, while some recent studies (Chen *et al.* 2022; Doss & Bänsch 2022; O'Connell *et al.* 2023; Zeng *et al.* 2023) have not introduced this external flow. The effect of the absence of the ventilation flow on evaporation should be sorted out, and there is need for a model that allows for calculations in situations both with and without a ventilation flow.

In our work, we investigate experimentally and numerically the coupling effect of the mass and heat transfer in the evaporation of acoustically levitated water–ethanol droplets. We measured comprehensively the variation of volume and surface temperature of droplets evaporating at low humidity (5 %) and without ventilation flow blowing off the outer streaming vortices. A numerical model using finite element methods is developed to simulate the evaporation process of a levitated spherical droplet. We derived an extended model to include the effects of the outer acoustic streaming, and added them to the numerical simulations through modified Sherwood and Nusselt numbers. The calculated results are compared with the experimental results to verify the accuracy. At the same time, the calculated results provide information on the concentration and temperature distribution of the droplets.

The paper is organised as follows. We first give details of the experimental method and materials in § 2. In § 3, we present our computational model for the evaporation of acoustic levitated droplets. Results related to the mass and heat transfer characteristics are described in § 4, including comparisons between the experiment and the model. The paper ends with conclusions and an outlook.

2. Experiments and materials

The experimental set-up of the current study is illustrated in figure 1(*a*). A coaxial acoustic levitator, consisting of a piezocrystal transducer (operating frequency 20.5 kHz) and a reflector, generates a standing acoustic wave with five nodes. In the experiment, the sample fluid is placed at the middle pressure node and is forced upwards by the acoustic radiation pressure to counterbalance the gravity force. The droplet is generated by a syringe pump (Harvard Apparatus PHD ULTRA) with a 15-gauge stainless steel needle. The initial volume of the droplet is controlled by the flow rate and the injection time to be 1.481 mm^3, which is equivalent to an effective diameter square $D^2 = 2 \text{ mm}^2$. The temperature of the droplets released from the needle will be lower than the ambient temperature due to the evaporative cooling during the generation process. This temperature reduction is justified to have a negligible effect on the experimental results, and the variation in droplet composition during the droplet generation process is also negligible. The levitated droplet has an oblate spheroidal shape, with an aspect ratio of the droplet contour $k = a/b$, where a is the longer axis, and b is the shorter axis, of the projected ellipse (see figure 1*b*). For the present study, the aspect ratio is limited to less than 1.2 to take advantage of the small sphere assumption (Yarin *et al.* 1998, 1999).

The experiments are conducted in a closed chamber with nitrogen flow input to maintain the ambient humidity at 5 %. The humidity is controlled at a very low level during the evaporation process to minimise the effects of water vapour condensation (Li *et al.* 2023). Once the humidity reaches 5 %, the nitrogen input flow rate is reduced to maintain a basic positive pressure, preventing the entry of high humidity air. The gas temperature in the chamber is controlled at $25 \pm 0.5\,^\circ\text{C}$. During the experiments, a sensor (KS-SHTE1KT, Keshun Ltd.) with an accuracy of $\pm 0.2\,^\circ\text{C}$ for temperature and $\pm 2\,\%$ RH for humidity is used to sample the temperature and the humidity of the gas.

A CCD camera (Ximea XiD) captures the volume variation of the droplet during evaporation using backlighting, and the surface temperature variation of the droplet is measured by an infrared camera (Telops FAST L200) through a high-transmittance germanium glass window (transmittance = 0.95). Figures 1(*b*) and 1(*c*) display the captured CCD and infrared camera images, respectively. The infrared measurement is calibrated using liquid surfaces with temperatures controlled by a water bath. The objective temperature when measuring a droplet's surface temperature is determined as
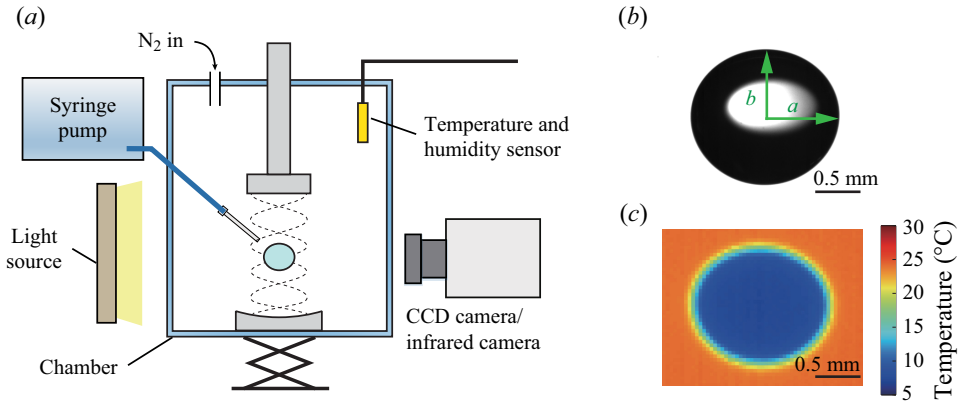
Figure 1. (*a*) Schematic of the experimental set-up for studying the evaporation of an acoustically levitated droplet at controlled temperature and humidity. (*b*) Image of the levitated droplet obtained by the CCD camera, where *a* is the longer axis, and *b* is the shorter axis, of the projected ellipse. (*c*) The temperature field obtained by the infrared camera. The scale bar relates to 0.5 mm.

		Water		Ethanol	
		10 °C	25 °C	10 °C	25 °C
Liquid density ρ	kg m^{-3}	999.7	997.0	798.1	785.0
Latent heat h_{fg}	kJ kg^{-1}	2477.2	2441.7	1043.8	1025.5
Saturation pressure P_{sat}	kPa	1.23	3.17	3.14	7.89
Diffusion coefficient D	10^{-5} m^2 s^{-1}	2.5		1.35	
Molecular weight MW	g mol^{-1}	18.02		46.07	

Table 1. Properties of test liquids at 10 °C and 25 °C.

the minimum temperature within the area of the droplet. This methodology is in line with previous papers (Sasaki *et al.* 2020).

Droplets used in the experiments are binary mixtures composed of ultra-pure water (prepared by a Milli-Q purification system from Merck, Germany) and ethanol (General-Reagent, 99.7 %). Solutions of different volume fractions of ethanol (0 %, 25 %, 50 %, 75 %, 100 %) are prepared at a constant room temperature 25 °C. Table 1 presents the physicochemical properties of the two components at 10 °C and 25 °C.

3. Calculation model

In this section, we present our calculation model for simulating the evaporation of an acoustically levitated bicomponent droplet. Since the aspect ratio k of the droplet shape is close to 1, we assume a spherically symmetric droplet with radius R_d, and neglect the internal circulation flow in the droplet. This assumption is not valid for droplets with aspect ratio $k > 1.25$, when droplets are ellipsoidal and strong internal flows are observed experimentally (Yarin *et al.* 1999; Yamamoto *et al.* 2008; Sasaki *et al.* 2019). The effect of the acoustic field on droplet evaporation is considered by introducing modified Nusselt and Sherwood numbers for heat and mass transfer, which will be presented in § 3.2.

3.1. *Heat and mass transfer equations*

The calculation is performed using an in-house finite element framework based on OOMPH-LIB (Heil & Hazel 2006) for droplet evaporation, which takes into account both species and temperature gradients within the droplet. A comprehensive explanation of this finite element model can be found in Diddens *et al.* (2017) and Diddens (2017).

In the gaseous phase, the distribution of the vapour mass fraction c_i, with $i = w$ for water and $i = e$ for ethanol, is described using the following modified diffusion equation that considers the effect of convection in the acoustic field by introducing the effective Sherwood number $Sh_{eff,i}$:

$$\frac{\partial c_i}{\partial t} = \frac{Sh_{eff,i}}{2} D_i^g \frac{1}{r^2} \frac{\partial}{\partial r}\left(r^2 \frac{\partial c_i}{\partial r}\right). \tag{3.1}$$

Here, D_i^g is the mass diffusion coefficient of component i in the gaseous phase. The $Sh_{eff,i}$ here represents an average effect of the acoustic streaming convection on the concentration field. When $Sh_{eff,i} = 2$, (3.1) is equivalent to the equation for pure diffusive evaporation. The calculation of $Sh_{eff,i}$ will be illustrated in detail in § 3.2. To solve (3.1), boundary conditions at the liquid–gas interface $r = R_d$ and at $r \to \infty$ have to be imposed. The vapour concentration at the interface, $c_{s,i}$, is calculated as

$$c_{s,i} = \gamma_i x_i^l \frac{MW_i p_{sat,i}}{RT_s}. \tag{3.2}$$

Here, x_i^l is the mole fraction of the liquid phase component i, MW_i the molecular weight, and $p_{sat,i}$ the saturation vapour pressure of the pure component i as a function of T_s, which is the temperature evaluated at the interface. Also, γ_i is the activity coefficient calculated by the thermodynamic model AIOMFAC (Zuend *et al.* 2008). At far field ($r \to \infty$), the vapour concentration of water relates to the humidity ϕ of the surrounding gas:

$$c_{\infty,w} = \phi \frac{MW_w p_{sat,w}}{RT_\infty}, \tag{3.3}$$

while there is no ethanol in the surrounding gas, i.e. $c_{\infty,e} = 0$.

In the liquid phase, the mass fraction of the components y_i^l is governed by the following diffusion–convection equation:

$$\rho^l\left(\frac{\partial y_i^l}{\partial t} + u \frac{\partial y_i^l}{\partial r}\right) = \frac{1}{r^2} \frac{\partial}{\partial r}\left(r^2 \rho^l D_i^l \frac{\partial y_i^l}{\partial r}\right) - J_i^l \delta_{lg}. \tag{3.4}$$

Here, ρ_l is the liquid density, which is allowed to depend on the composition. Due to the changing mass density of the liquid mixture during the evaporation process, the radial velocity u can be non-zero, and in order to conserve the species masses, the radial advection term $u \partial y_i^l / \partial r$ must be considered. The radial velocity u is calculated to be less than 5×10^{-8} m s^{-1} throughout the evaporation process, and has little effect on the specific mass and heat transfer. Here, D_i^l is the diffusion coefficient in the liquid phase, and the $J_i^l \delta_{lg}$ term represents a source/sink term at the droplet interface, where δ_{lg} is the interface delta function, and J_i^l is the diffusive flux in the liquid phase calculated by (3.7) in Diddens *et al.* (2017).

During evaporation, the droplet gets cooled down due to the evaporation at the interface, which in turn affects the evaporation rate by the virtue of (3.2). At the same time, the

temperature field of the gas may also vary. To study this, we calculate the temperature distribution in both the liquid and gas phases using the energy equation

$$\rho c_p \left(\frac{\partial T}{\partial t} + u \frac{\partial T}{\partial r} \right) = \frac{1}{r^2} \frac{\partial}{\partial r} \left(r^2 \lambda \frac{\partial T}{\partial r} \right) - \left(j_w^{lg} \Lambda_w + j_e^{lg} \Lambda_e \right) \delta_{lg}, \qquad (3.5)$$

where the density ρ, the specific heat capacity c_p, and the thermal conductivity λ are differentiated in the gas and liquid phases. Here, j_e and j_w are the mass transfer rates of ethanol and water, respectively, and Λ_e and Λ_w denote the corresponding latent heats of evaporation. The λ value in the gaseous phase is adjusted by a Nusselt number Nu to consider the effect of acoustic streaming, i.e. $\lambda_g = (Nu_{eff}/2)\lambda_{air}$, where λ_{air} is the thermal conductivity of air. The calculation of the Nusselt number will be introduced in the next subsection.

The boundary and initial conditions of the calculation problem are set as

at infinity ($r = \infty$), $c_w = c_{\infty,w}$ from (3.3), $c_e = 0$, $T = T_0 = 25\,^\circ\text{C}$.   (3.6a–c)

Regarding the initial conditions, as stated in § 2, the generation process of the droplet has a negligible effect on the experimental results, so we assume that the droplet evaporates from room temperature ($25\,^\circ\text{C}$) and the set volume concentration. We define the set volume concentration of the component i in the liquid mixture as φ_i. When $t = 0$,

in liquid phase ($0 < r < R_d$), $y_i^l = \dfrac{\rho_i^l \varphi_i}{\rho_1^l \varphi_1 + \rho_2^l \varphi_2}$, $T = T_0$;   (3.7a,b)

in gaseous phase ($R_d < r < \infty$), $c_w = c_{\infty,w}$, $c_e = 0$, $T = T_0$.   (3.8a,b)

3.2. *Effect of acoustic streaming*

Acoustic levitation is known to generate secondary flow circulations around the droplet, which is called acoustic streaming. A detailed theoretical analysis of this secondary flow is provided by Yarin *et al.* (1998, 1999). Consequently, the acoustic field influences the droplet's evaporation in two ways: the introduction of convection at the acoustic boundary layer close to the droplet (inner acoustic streaming), and the formation of large-scale toroidal vortices about the droplet (outer acoustic streaming), which affects the far-field conditions. Figure 2(*a*) shows a schematic diagram of the flow field surrounding the droplet. Note that previous studies utilise an axial airflow to ventilate the accumulated vapour in the outer streaming vortices (Yarin *et al.* 1999; Schiffter & Lee 2007; Al Zaitone & Tropea 2011), allowing for direct use of the equations for inner convection (3.9). However, our study will focus on the effect of the entire flow field generated by the acoustic levitation method, including both inner and outer acoustic streaming, on the droplet evaporation.

For the inner acoustic streaming region, the mass transfer of the acoustic streaming flow can be characterised by the average Sherwood number by Yarin *et al.* (1999):

$$Sh_{0,i} = 1.89 \frac{B_i}{\left(\omega \mathcal{D}_i^g \right)^{1/2}}. \qquad (3.9)$$

Here, ω is the angular frequency of the sound vibration, $\mathcal{D}_i^g$ is the mass diffusion coefficient of the component i in the gas phase, and $B_i = A_{0e,i}/\rho_0 c_0$ is an acoustic velocity scale of component i, where $A_{0e,i}$, ρ_0, c_0 are the effective pressure amplitude of the acoustic field, unperturbed gas density and the sound velocity. The effective pressure
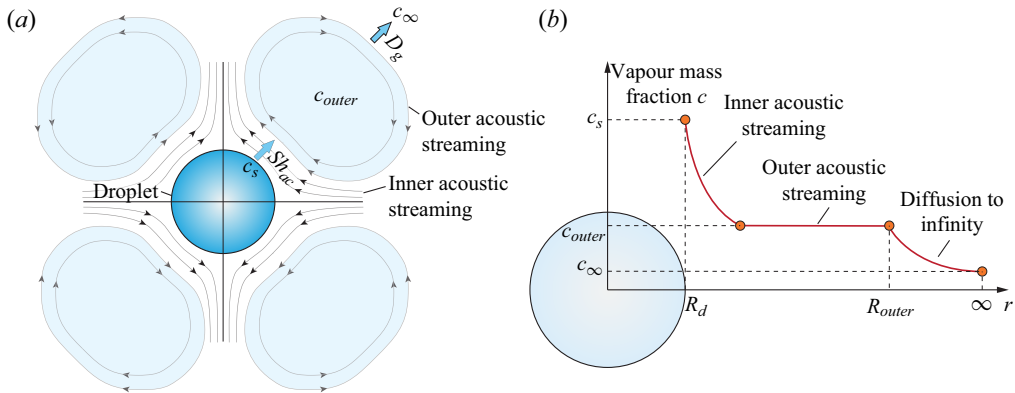
Figure 2. The evaporation model: (*a*) schematic of the flow field outside the acoustic levitated droplet; (*b*) distribution of the vapour mass fraction *c* with radius *r*.

amplitude $A_{0e,i}$ will significantly affect the evaporation rate of the droplet according to Junk *et al.* (2020), which can also be derived from (3.9). We have maintained a stable value of A_{0e} in our experiments, which can be obtained via (5.6) in Yarin *et al.* (1998) through obtaining the critical levitator power for dropout: $A_{0e,w} = 5521$ N m^{-2} for water, and $A_{0e,e} = 5850$ N m^{-2} for ethanol.

The heat transfer of the streaming flow is characterised by the Nusselt number calculated in the similar form:

$$Nu_0 = 1.89 \frac{\bar{B}}{(\omega \alpha^g)^{1/2}}. \tag{3.10}$$

Here, α^g is the thermal diffusivity of air, and $\bar{B}$ is the acoustic velocity scale averaged according to the component mass fraction in the liquid.

Due to the intense, rapid mixing in the vortices, the outer streaming region is assumed to have a uniform temperature T_{outer} and uniform vapour concentration field $c_{i,outer}$ for species *i*. This can be justified by comparing the circulation time scale with the diffusion time according to Kronig & Brink (1951), i.e. by examining the heat and mass Péclet numbers:

$$Pe_{mass} = \frac{Lu}{D}, \quad Pe_{heat} = \frac{Lu}{\alpha}, \tag{3.11a,b}$$

where the circulation velocity in the vortex *u* is approximately 50 mm s^{-1} according to Kobayashi *et al.* (2018), the length scale of the vortex is $L \approx 10^{-2}$ m, and the diffusion coefficient *D* and the thermal diffusivity of the gas α are both of the order of 10^{-5} m^2 s^{-1}. Therefore, $Pe_{mass}, Pe_{heat} \approx 50$, indicating that the advection is much faster than the diffusion, supporting our assumption.

Figure 2(*b*) shows the distribution of the vapour mass concentration of component *i* as a function of radius *r*. The vapour concentration decreases rapidly from its peak at the gas–liquid interface, as a result of convection in the inner streaming region, and eventually reaches the outer streaming region, where a uniform concentration field is established by the vortices. At the edge of the outer region, the vapour components diffuse into the far field. Here, we assume that the outer streaming region is in an equilibrium stage for mass and heat transfer, where the mass and heat flow from the droplet to the outer streaming region are balanced by the mass and heat flow from the outer streaming region to the

surroundings. From that, we derive the following equations for the mass flow m_i and heat flow Q:

$$m_i = 2\pi R_d D_0 \, Sh_{0,i}(c_{s,i} - c_{outer,i}) = 4\pi R^* D_0(c_{outer,i} - c_{\infty,i}), \quad (3.12)$$

$$Q = 2\pi R_d \lambda \, Nu_0 \, (T_s - T_{outer}) = 4\pi R^* \lambda \, (T_{outer} - T_\infty). \quad (3.13)$$

Defining $k^* = R^*/R_d$, one can get the equations for $c_{outer,i}$ and T_{outer}:

$$c_{outer,i} = \frac{1}{1 + \dfrac{2k^*}{Sh_{0,i}}} \, c_{s,i} + \frac{1}{1 + \dfrac{Sh_{0,i}}{2k^*}} \, c_{\infty,i}, \quad T_{outer} = \frac{1}{1 + \dfrac{2k^*}{Nu}} \, T_s + \frac{1}{1 + \dfrac{Nu}{2k^*}} \, T_\infty.$$

$$(3.14a,b)$$

Substituting (3.14a,b) into (3.12) and (3.13), one can eliminate the parameters of the outer region and obtain

$$m_i = 2\pi R_d D_0 \frac{Sh_{0,i}}{1 + Sh_{0,i}/2k^*}(c_{s,i} - c_{outer,i}), \quad Q = 2\pi R_d \lambda \frac{Nu_0}{1 + Nu_0/2k^*} \, (T_s - T_{outer}).$$

$$(3.15a,b)$$

From this, we can define the effective Sherwood and Nusselt numbers that consider the effect of outer acoustic streaming:

$$Sh_{eff,i} = \frac{Sh_{0,i}}{1 + Sh_{0,i}/2k^*}, \quad Nu_{eff} = \frac{Nu_0}{1 + Nu_0/2k^*}. \quad (3.16a,b)$$

We first obtain the Sherwood and Nusselt numbers induced by the inner acoustic streaming, $Sh_{0,i}$ and Nu_0, through (3.9), and calculate the effective parameters accounting for the effects of the outer streaming, $Sh_{eff,i}$ and Nu_{eff}, through (3.16a,b). Then we implement the obtained $Sh_{eff,i}$ and Nu_{eff} into (3.2) and (3.5) for the numerical simulation.

4. Results and discussion

4.1. *Mass transfer*

To study the evaporation characteristics, we focus on the variation of the droplet volume by analysing the images captured by the CCD camera (see figure 1b). Figure 3(a) shows the temporal variation of the normalised surface area D^2/D_0^2 of droplets with different initial concentrations, where D is the volume equivalent diameter of the droplet, and D_0 is the initial value of D. The good agreement between the experimental (markers) and calculated (solid curves) results confirms the reliability of our model.

It is demonstrated that for pure water droplets, the diameter square D^2 remains linear with time under the influence of the acoustic field. This trend is consistent with the d^2 law, which focuses on the evaporation of pure, spherical droplets, and states that the diameter square decreases linearly with time, at a rate determined by the ambient properties (Sazhin 2014; Finneran, Garner & Nadal 2021). Since the slope of the D^2/D_0^2 curve is directly proportional to the Sherwood number, the linear variation of the curve confirms the assumption that the original evaporation equation can be modified in the acoustic field using a constant Sherwood number via (3.1). The Sherwood number of the inner acoustic streaming is approximately 15, calculated by (3.9), leading to an evaporation in the inner acoustic streaming of $Sh/2$, i.e. 7.5 times faster than in a pure diffusion scenario. Nevertheless, the droplet lifetime is reduced to only half that of pure diffusive
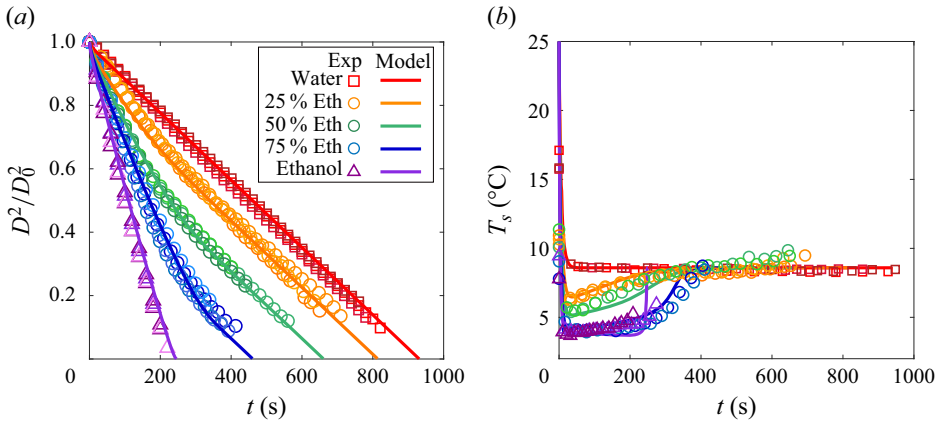
Figure 3. (*a*) Normalised surface area D^2/D_0^2 and (*b*) surface temperature T_s, versus time *t*, for various initial concentrations of the droplets with initial diameter square $D_0 = 1.414$ mm, evaporating under gas humidity RH $\approx 5\,\%$. Experimental results (markers) and model results (lines) are compared.
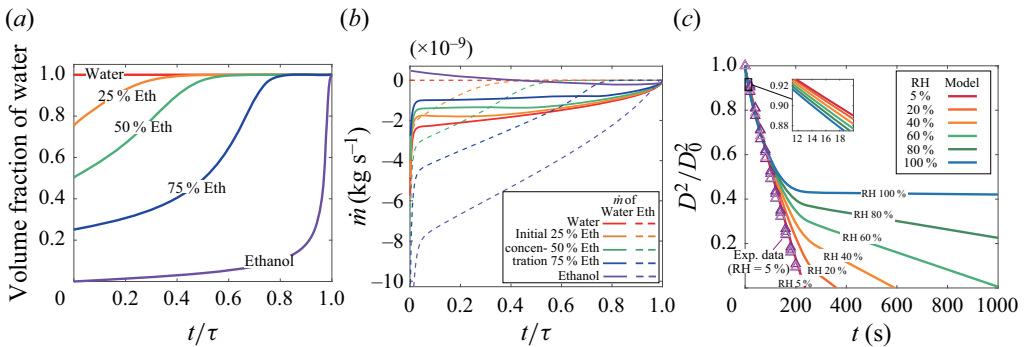

Figure 4. (*a*) Volume fraction of the water component in the droplet versus dimensionless time t/τ, where τ is the calculated lifetime of the droplet. (*b*) Temporal variation of the mass flow rate of water and ethanol with time for droplets with various initial ratios. (*c*) Effect of ambient gas humidity on the variation of normalised surface area D^2/D_0^2. Model results of gas humidity varying from 5 % to 100 % and experimental results of RH = 5 % are shown.

evaporation under the same ambient condition ($T_0 = 25\,^\circ\text{C}$, RH = 5 %). This is due to the accumulation of vapour substances in the outer vortices, which reduces the effective Sherwood number $Sh_{eff,i}$ to approximately 3. Therefore, both the inner and outer acoustic streaming have a significant effect on the evaporation. Equation (3.9) cannot be used to calculate the evaporation alone if there is no ventilation flow to eliminate the outer acoustic streaming (Yarin *et al.* 1999; Al Zaitone & Tropea 2011).

The D^2/D_0^2 curves of pure ethanol droplets follow a trend similar to that of water droplets, with their slope exceeding that of water droplets due to the higher saturation pressure and molecular weight of ethanol. It is noticeable that despite the low humidity, there is a slight bend at the end of the ethanol curve due to water condensation, which will be discussed in the subsequent paragraph. In the case of bicomponent droplets, the evaporation curves display a noticeable shift from a steeper to a gentler slope, corresponding to the variation of the component fractions in the droplet. From figure 4(*a*), we can see that the volume fraction of water increases during evaporation from the initial concentration to 1, regardless of the initial value. It can be obtained that the D^2/D_0^2 curves in figure 3(*a*) exhibit a transition point at the stage where water constitutes nearly

984 A17-9

95 % of the total volume of the droplet. Consequently, all droplets with varying initial concentrations become water droplets in the final stage of evaporation, thus the evaporation curves of the second stage run parallel to those of water droplets.

Focusing on the mass change rate of the two components in the evaporating droplets (see figure 4*b*), it is evident that as the initial concentration of ethanol increases, the mass rate of the ethanol component increases, while the mass rate of the water component decreases. As the rise in the evaporation rate of water cannot compensate for the decline in the evaporation rate of ethanol, droplets evaporate faster at higher ethanol concentrations, as demonstrated in figure 3(*a*). It can also be seen that for bicomponent droplets, the evaporation rate of water is comparable to that of ethanol throughout the evaporation process, justifying that the role of water evaporation cannot be ignored, even if the water fraction is small. At extremely low initial water concentrations, particularly in the case of pure ethanol droplets, the interfacial vapour pressure of the water is insufficient to overcome the ambient vapour pressure, leading to condensation of the moisture on the droplet surface. Consequently, the mass rate of water in the ethanol droplet is initially positive, and evaporation losses are slightly offset. If the humidity level increases, then condensation will intensify, resulting in a more complex trend of the D^2 curve (Sasaki *et al.* 2020; Yang *et al.* 2023). Figure 4(*c*) illustrates the effect of the ambient gas humidity on the evaporation rate. Model results demonstrate that there are distinct transitions in the slope of the D^2 curves, with curves having a similar trend in the first stage ($D^2/D_0^2 > 0.6$), and the slopes decreasing with increasing humidity in the second stage ($D^2/D_0^2 < 0.6$). In addition, we find that the higher the ambient humidity, the faster the evaporation rate in the first stage ($D^2/D_0^2 > 0.6$), as depicted in the inset of figure 4(*c*). This can be attributed to the condensation of water compensating for the heat consumption caused by evaporative cooling, which enables the ethanol component to evaporate at a higher temperatures (Li *et al.* 2023).

4.2. *Heat transfer*

Referring to heat transfer characteristics during the evaporation process, figure 3(*b*) displays the droplet surface temperature T_s over time. It can be seen that a pure water droplet maintains a constant surface temperature ($\approx 8.5\,^\circ$C) after initially cooling down, signifying that it reaches an equilibrium between cooling by evaporation and heat transfer from the surrounding gas. The temperature variation of the ethanol droplet follows a similar trend, with the surface temperature after initial cooling ($\approx 3.5\,^\circ$C) being lower than that of a water droplet due to its greater evaporation rate. Furthermore, the ethanol droplet reaches the same surface temperature as a pure water droplet in the end, as a result of the condensation of water vapour onto the droplet. For bicomponent droplets, the surface temperature initially decreases rapidly to a minimum level, which is lower than that of a pure water droplet, before increasing slowly to eventually reach the same surface temperature as the water droplet. Increasing the ethanol concentration reduces the minimum temperature of the droplet, yet it is still higher than that of a pure ethanol droplet. Furthermore, the fact that all kinds of droplets reach a similar temperature at the end is consistent with our conclusion in § 4.1 that water becomes the dominant component at the end of the evaporation process, regardless of the initial concentration ratio.

From our experimental results, we are able to calculate the heat transfer coefficient for an evaporating pure droplet using the energy conservation law:

$$\rho_L c_p \frac{\mathrm{d}(VT_s)}{\mathrm{d}t} = hA\,(T_\infty - T_s) + \rho_L L \frac{\mathrm{d}V}{\mathrm{d}t}. \tag{4.1}$$
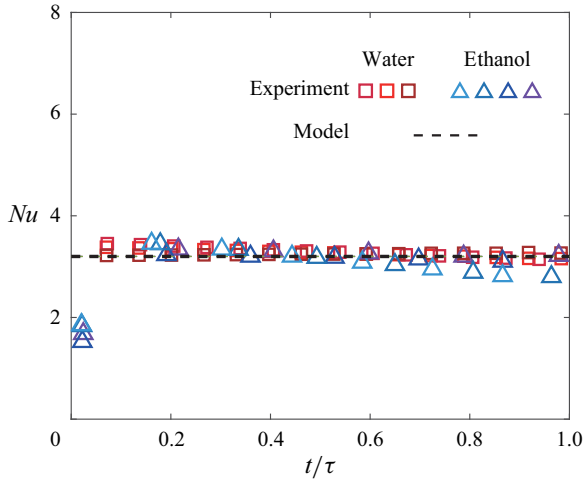
Figure 5. Nusselt number *Nu* calculated through experimental results (markers) and model (dashed line) for pure water and ethanol droplets. Here, τ relates to the lifetime of the droplet.

Here, ρ_L is the density of the liquid, c_p is the specific heat capacity at constant temperature, L is the latent heat of the liquid, and T_∞ is the surrounding gas temperature. Also, V, A, T_s are the droplet volume, droplet surface area and surface temperature, respectively, and can be obtained from experimental results. Here, we assume a uniform temperature field within the droplet, which is supported by our numerical results discussed in § 4.3. Equation (4.1) can be solved for the heat transfer coefficient h, thus the Nusselt number Nu can be calculated by

$$Nu = \frac{2R_d h}{\lambda} = \frac{2R_d \rho_L \left(c_p \dfrac{\mathrm{d}(VT_s)}{\mathrm{d}t} - L \dfrac{\mathrm{d}V}{\mathrm{d}t} \right)}{\lambda A \left(T_\infty - T_s \right)}. \tag{4.2}$$

Here, $R_d = D/2$ is the volume equivalent radius of the droplet. When calculating the Nusselt number for the evaporation of ethanol droplets, we neglect the condensation of water vapour because at such a low humidity (RH = 5 %), the role of condensation heat is very small. Figure 5 shows the temporal variation of Nu for water and ethanol droplets calculated directly from experimental data (markers) with the model calculation (dashed line). Except for the initial stage, the Nusselt number remains approximately constant during evaporation. The experimental results calculated via (3.16*a*,*b*) are in agreement with the experimental data calculated via (4.2), demonstrating the validity of our model.

4.3. *Temperature and concentration distribution*

With the calculated results, we are able to obtain specific parameter distributions within the droplet. Figure 6(*a*) displays the distribution of ethanol concentration and liquid temperature for a droplet with an initial ethanol volume fraction of 50 % at $t = 130$ s. The complete variation of the concentration and temperature field during the evaporation process is displayed in the supplementary movie available at https://doi.org/10.1017/jfm. 2024.204. The temporal variations of the concentration and temperature fields within the droplet are shown in figures 6(*b*) and 6(*c*), respectively. It is evident that the temperature maintains uniformity throughout the evaporation (with a temperature difference of less
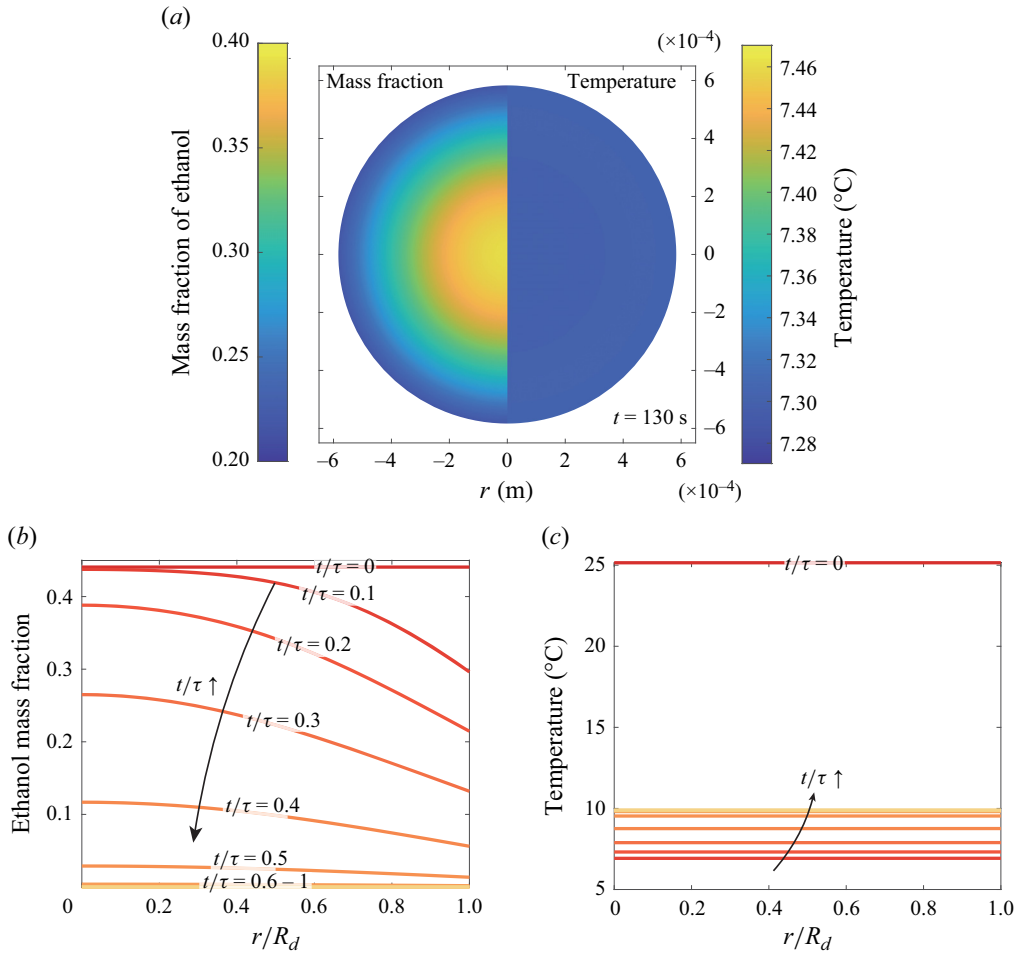
Figure 6. (*a*) For a droplet with initial ethanol volume fraction 50 %, distribution of ethanol mass fraction and temperature of the droplet at $t = 130$ s ($t/\tau = 0.2$). (*b*) Temporal variation of ethanol mass fraction and (*c*) temperature distribution within the droplet, as functions of dimensionless radius r/R_d, where R_d is the equivalent radius of the droplet.

than $0.01\,^{\circ}$C), while the concentration field shows significant inhomogeneity near the droplet interface at the start, with the gradient decreasing over time. We use the Biot number to study the uniformity of the internal concentration and temperature fields during evaporation. According to the definition, there exists a relationship between the mass transfer Biot number Bi_m and the heat transfer Biot number Bi_q with Sherwood and Nusselt numbers: $Bi_m = Sh\,(D_g/D_l)$ and $Bi_q = Nu\,(k_g/k_l)$. Here, Bi_m is calculated to be of the order of 10^2, indicating that evaporation losses at the droplet interface cannot be compensated by species transport from the interior of the droplet, resulting in an inhomogeneous concentration field. On the other hand, Bi_q is of the order of 0.1, allowing the temperature field to remain uniform at all times. Comparing the characteristic time scales of heat transfer and component diffusion with the time scale of droplet evaporation also gives consistent conclusions (Yarin *et al.* 2002).

As a result, the non-uniformity of the concentration field within the droplet must be taken into account in the modelling, while the temperature field can be considered

984 A17-12

homogeneous to simplify the calculation. However, our model does not take into account the effect caused by the internal circulation flow inside the droplet, so the generality of this conclusion needs to be demonstrated further.

5. Conclusions

In this study, we carried out a systematic measurement of the evaporation characteristics of acoustically levitated droplets with varying initial concentrations. The evaporation process was modelled using an in-house finite element method framework, and included the effects of both convective flow of the inner acoustic region and vortices of the outer acoustic region. By comparing the experimental and numerical results, it was shown that constant Sherwood and Nusselt numbers for mass and heat transfer can describe droplet evaporation under acoustic levitation. Both the inner and outer acoustic streaming contribute considerably to the mass and heat transfer, resulting in the effective parameters $Sh_{eff,i}$, $Nu_{eff} \approx 3$. Additionally, the analysis of the concentration and temperature fields within the droplet confirmed the importance of considering the concentration gradient within the droplet.

In forthcoming research, it is intended that the acoustic field equations should replace the analytical solutions in order to fully calculate the flow field around the droplet. The numerical simulation should be extended to two or three dimensions for a thorough assessment of the internal flow of the droplet. Additionally, explorations could focus on immiscible components and phase separation processes to enhance practical applications (Tan *et al.* 2016; Diddens *et al.* 2017; Lyu *et al.* 2021).

Supplementary movie. A supplementary movie is available at https://doi.org/10.1017/jfm.2024.204.

Declaration of interests. The authors report no conflict of interest.

Author ORCIDs.

ⓘ Yuki Wakata https://orcid.org/0000-0002-0393-9078;

ⓘ Xing Chao https://orcid.org/0000-0003-2574-4148;

ⓘ Chao Sun https://orcid.org/0000-0002-0930-6343;

ⓘ Christian Diddens https://orcid.org/0000-0003-2395-9911.

REFERENCES

AL ZAITONE, B. 2018 Oblate spheroidal droplet evaporation in an acoustic levitator. *Intl J. Heat Mass Transfer* **126**, 164–172.

AL ZAITONE, B. & TROPEA, C. 2011 Evaporation of pure liquid droplets: comparison of droplet evaporation in an acoustic field versus glass-filament. *Chem. Engng Sci.* **66** (17), 3914–3921.

ANDRADE, M.A.B., PÉREZ, N. & ADAMOWSKI, J.C. 2018 Review of progress in acoustic levitation. *Braz. J. Phys.* **48**, 190–213.

BÄNSCH, E. & GÖTZ, M. 2018 Numerical study of droplet evaporation in an acoustic levitator. *Phys. Fluids* **30** (3), 037103.

BRENN, G., DEVIPRASATH, L.J., DURST, F. & FINK, C. 2007 Evaporation of acoustically levitated multi-component liquid droplets. *Intl J. Heat Mass Transfer* **50** (25–26), 5073–5086.

CHEN, H., LI, A., ZHANG, Y., ZHANG, X. & ZANG, D. 2022 Evaporation and liquid-phase separation of ethanol–cyclohexane binary drops under acoustic levitation. *Phys. Fluids* **34** (9), 092108.

DIDDENS, C. 2017 Detailed finite element method modeling of evaporating multi-component droplets. *J. Comput. Phys.* **340**, 670–687.

DIDDENS, C., LI, Y. & LOHSE, D. 2021 Competing Marangoni and Rayleigh convection in evaporating binary droplets. *J. Fluid Mech.* **914**, A23.

DIDDENS, C., TAN, H., LV, P., VERSLUIS, M., KUERTEN, J.G.M., ZHANG, X. & LOHSE, D. 2017 Evaporating pure, binary and ternary droplets: thermal effects and axial symmetry breaking. *J. Fluid Mech.* **823**, 470–497.

DOSS, M. & BÄNSCH, E. 2022 Numerical study of single droplet drying in an acoustic levitator before the critical point of time. *Chem. Engng Sci.* **248**, 117149.

FINNERAN, J., GARNER, C.P. & NADAL, F. 2021 Deviations from classical droplet evaporation theory. *Proc. R. Soc. Lond.* A **477** (2251), 20210078.

FUCHS, N.A. 1959 *Evaporation and Droplet Growth in Gaseous Media*. Pergamon.

HEIL, M. & HAZEL, A.L. 2006 oomph-lib – an object-oriented multi-physics finite-element library. *Lect. Notes Comput. Sci. Engng* **53**, 19–49.

JUNK, M., HINRICHS, J., POLT, F., FECHNER, J. & PAUER, W. 2020 Quantitative experimental determination of evaporation influencing factors in single droplet levitation. *Intl J. Heat Mass Transfer* **149**, 119057.

KOBAYASHI, K., GODA, A., HASEGAWA, K. & ABE, Y. 2018 Flow structure and evaporation behavior of an acoustically levitated droplet. *Phys. Fluids* **30** (8), 082105.

KRONIG, R. & BRINK, J.C. 1951 On the theory of extraction from falling droplets. *Appl. Sci. Res.* **2**, 142–154.

LAW, C.K. & LAW, H.K. 1982 A d^2-law for multicomponent droplet vaporization and combustion. *AIAA J.* **20** (4), 522–527.

LEE, C.P. & WANG, T.G. 1990 Outer acoustic streaming. *J. Acoust. Soc. Am.* **88** (5), 2367–2375.

LI, M., LOHSE, D. & HUISMAN, S.G. 2023 High humidity enhances the evaporation of non-aqueous volatile sprays. *J. Fluid Mech.* **956**, A19.

LIEBER, C., MELEKIDIS, S., KOCH, R. & BAUER, H. 2021 Insights into the evaporation characteristics of saliva droplets and aerosols: levitation experiments and numerical modeling. *J. Aerosol Sci.* **154**, 105760.

LIERKE, E.G. 1996 Akustische positionierung-ein unfasser uberblick über grundlagen und anwendungen. *Acustica* **82** (2), 220–237.

LOHSE, D. 2022 Fundamental fluid dynamics challenges in inkjet printing. *Annu. Rev. Fluid Mech.* **54**, 349–382.

LYU, S., TAN, H., WAKATA, Y., YANG, X., LAW, C.K., LOHSE, D. & SUN, C. 2021 On explosive boiling of a multicomponent Leidenfrost drop. *Proc. Natl Acad. Sci. USA* **118** (2), e2016107118.

MAQUA, C., CASTANET, G., GRISCH, F., LEMOINE, F., KRISTYADI, T. & SAZHIN, S.S. 2008 Monodisperse droplet heating and evaporation: experimental study and modelling. *Intl J. Heat Mass Transfer* **51** (15–16), 3932–3945.

MAXWELL, J.C. 1877 Diffusion. *Encyclopaedia Britannica, 9th edn* **7**, 214–221.

O'CONNELL, R.A., SHARRATT, W.N. & CABRAL, J.T. 2023 Breath figure assembly on evaporating polymer solution droplets in levitation. *Phys. Rev. Lett.* **131**, 218101.

RILEY, N. 2001 Steady streaming. *Annu. Rev. Fluid Mech.* **33** (1), 43–65.

SASAKI, Y., HASEGAWA, K., KANEKO, A. & ABE, Y. 2020 Heat and mass transfer characteristics of binary droplets in acoustic levitation. *Phys. Fluids* **32** (7), 072102.

SASAKI, Y., KOBAYASHI, K., HASEGAWA, K., KANEKO, A. & ABE, Y. 2019 Transition of flow field of acoustically levitated droplets with evaporation. *Phys. Fluids* **31** (10), 102109.

SAZHIN, S. 2014 *Droplets and Sprays*. Springer.

SCHIFFTER, H. & LEE, G. 2007 Single-droplet evaporation kinetics and particle formation in an acoustic levitator. Part 1: evaporation of water microdroplets assessed using boundary-layer and acoustic levitation theories. *J. Pharm. Sci.* **96** (9), 2274–2283.

SHI, W.T. & APFEL, R.E. 1996 Deformation and position of acoustically levitated liquid drops. *J. Acoust. Soc. Am.* **99** (4), 1977–1984.

SIRIGNANO, W.A. 1983 Fuel droplet vaporization and spray combustion theory. *Prog. Energy Combust. Sci.* **9** (4), 291–322.

SIRIGNANO, W.A. 2010 *Fluid Dynamics and Transport of Droplets and Sprays*. Cambridge University Press.

TAN, H., DIDDENS, C., LV, P., KUERTEN, J.G.M., ZHANG, X. & LOHSE, D. 2016 Evaporation-triggered microdroplet nucleation and the four life phases of an evaporating ouzo drop. *Proc. Natl Acad. Sci. USA* **113** (31), 8642–8647.

TIAN, Y., HOLT, R.G. & APFEL, R.E. 1993 Deformation and location of an acoustically levitated liquid drop. *J. Acoust. Soc. Am.* **93** (6), 3096–3104.

TONINI, S. & COSSALI, G.E. 2012 An analytical model of liquid drop evaporation in gaseous environment. *Intl J. Therm. Sci.* **57**, 45–53.

TONINI, S. & COSSALI, G.E. 2013 An exact solution of the mass transport equations for spheroidal evaporating drops. *Intl J. Heat Mass Transfer* **60**, 236–240.

Tonini, S. & Cossali, G.E. 2019 An analytical approach to model heating and evaporation of multicomponent ellipsoidal drops. *Heat Mass Transfer* **55**, 1257–1269.

Trinh, E.H. & Robey, J.L. 1994 Experimental study of streaming flows associated with ultrasonic levitators. *Phys. Fluids* **6** (11), 3567–3579.

Wang, Z., Orejon, D., Takata, Y. & Sefiane, K. 2022 Wetting and evaporation of multicomponent droplets. *Phys. Rep.* **960**, 1–37.

Yamamoto, Y., Abe, Y., Fujiwara, A., Hasegawa, K. & Aoki, K. 2008 Internal flow of acoustically levitated droplet. *Microgravity Sci. Technol.* **20**, 277–280.

Yang, L., Pahlavan, A.A., Stone, H.A. & Bain, C.D. 2023 Evaporation of alcohol droplets on surfaces in moist air. *Proc. Natl Acad. Sci. USA* **120** (38), e2302653120.

Yarin, A.L., Brenn, G., Kastner, O., Rensink, D. & Tropea, C. 1999 Evaporation of acoustically levitated droplets. *J. Fluid Mech.* **399**, 151–204.

Yarin, A.L., Brenn, G. & Rensink, D. 2002 Evaporation of acoustically levitated droplets of binary liquid mixtures. *Intl J. Heat Fluid Flow* **23** (4), 471–486.

Yarin, A.L., Pfaffenlehner, M. & Tropea, C. 1998 On the acoustic levitation of droplets. *J. Fluid Mech.* **356**, 65–91.

Zang, D., Tarafdar, S., Tarasevich, Y.Y., Choudhury, M.D. & Dutta, T. 2019 Evaporation of a droplet: from physics to applications. *Phys. Rep.* **804**, 1–56.

Zang, D., Yu, Y., Chen, Z., Li, X., Wu, H. & Geng, X. 2017 Acoustic levitation of liquid drops: dynamics, manipulation and phase transitions. *Adv. Colloid Interface Sci.* **243**, 77–85.

Zeng, H., Wakata, Y., Chao, X., Li, M. & Sun, C. 2023 On evaporation dynamics of an acoustically levitated multicomponent droplet: evaporation-triggered phase transition and freezing. *J. Colloid Interface Sci.* **648**, 736–744.

Zuend, A., Marcolli, C., Luo, B.P. & Peter, T. 2008 A thermodynamic model of mixed organic–inorganic aerosols to predict activity coefficients. *Atmos. Chem. Phys.* **8** (16), 4559–4593.